Research Paper

Peculiar microstructural evolution and hardness variation depending on laser powder bed fusion-manufacturing condition in Ti–6Al–2Sn–4Zr–6Mo

Prince Valentine Cobbinah [a],[**], Sae Matsunaga [a], Yoshiaki Toda [b], Ryosuke Ozasa [c], Masayuki Okugawa [c], Takuya Ishimoto [c],[d], Yuheng Liu [c], Yuichiro Koizumi [c], Pan Wang [e], Takayoshi Nakano [c],[*], Yoko Yamabe-Mitarai [a],[***]

[a] Department of Advanced Materials Science, Graduate School of Frontier Sciences, The University of Tokyo, 5-1-5 Kashiwanoha, Kashiwa, Chiba, 277-8561, Japan
[b] Research Center for Structural Materials, National Institute for Materials Science, 1-2-1 Sengen, Tsukuba, Ibaraki, 305-0047, Japan
[c] Division of Materials and Manufacturing Science, Graduate School of Engineering, Osaka University, 2-1 Yamadaoka, Suita, Osaka, 565-0871, Japan
[d] Aluminium Research Center, University of Toyama, 3190 Gofuku, Toyama, 930-8555, Japan
[e] Singapore Institute of Manufacturing Technology (SIMTech), Agency for Science, Technology and Research (A*STAR), 5 Cleantech Loop, 636732, Singapore

ARTICLE INFO

ABSTRACT

This study aims to comprehensively analyze the phase and microstructure evolution and related hardness variations of the Ti–6Al–2Sn–4Zr–6Mo wt.% (Ti6246) alloy produced by laser powder bed fusion (LPBF) under various laser conditions and to gain insight into the mechanisms of these changes using numerical thermal analysis. Higher laser volumetric densities (VEDs) resulted in a finer α/α' microstructure and increased hardness, exhibiting a positive correlation with the VED, except under extremely high conditions. This contrary trend, reported for the first time, is attributed to the solid-phase transformation from the β phase to metastable α' martensite during LPBF induced by rapid cooling. Despite the finer microstructure, the samples under very high VED conditions showed lower hardness, deviating from the overall trend. The X-ray diffraction peaks in the high-VED samples suggested a partial decomposition of α' to α + β owing to laser-induced reheating of the underlying layers, which is considered a contributing factor to the hardness reduction. The numerical analysis showed that the underlying layer was exposed to high temperatures for a relatively long time under high-VED conditions. It was revealed that the hardness of LPBF-fabricated Ti6246 was influenced by unique thermal processes: rapid cooling and reheating of the pre-solidified part, leading to the formation of a metastable α' phase and partial decomposition into α + β. These findings provide insights for tailoring Ti6246 with desired physical properties via LPBF.

1. Introduction

The aerospace industry has recently attracted considerable interest for maximizing the use of additive manufacturing (AM) in fabricating the required functional parts of turbine engines [1,2]. Laser powder bed fusion (LPBF) is a keenly researched AM technology [3]. Compared with other AM technologies, LPBF produces parts with better surface quality [1], uses materials efficiently, and offers microstructural and texture control [4–6]. Additionally, the geometric freedom and dimensional control provided by the LPBF process facilitates the fabrication of complex-shaped parts with precision [7], which is critical in the aerospace industry.

Ti alloys exhibit allotropic behavior, presenting a challenge to the LPBF process despite their low strength-to-weight ratio, excellent high-temperature strength, and exceptional corrosion resistance. Ti exists as a hexagonal close-packed (hcp) crystal structure α phase at room temperature and transforms into a body-centered cubic (bcc) β phase at elevated temperatures. The formation, stability, and morphology of α/β phases depend on the Ti alloy composition, processing route, and cooling rate [8,9]. Furthermore, depending on the α/β relative

quantities, Ti alloys can be classified as α, near-α, α+β, near-β, metastable β, or stable β alloys [8,9]. Studies on the LPBF processability involving Ti alloys have primarily focused on stable single α and β alloys [10–13]. The well-known Ti–6Al–4V wt. % alloy, which belongs to the α+β class, has also been studied [14–16]. However, the α+β phase region has other established alloys that are used in the aerospace industry. One example is the Ti–6Al–2Sn–4Zr–6Mo wt.% (Ti6246) alloy, which is used in the intermediate section of turbine engines for components such as compressor blades, fan disks, seals, and airframe parts [17]. Ti6246, although an α+β alloy, is technically considered a near-β alloy owing to its proximity to the β phase boundary. Additionally, Ti6246 constitutes a more stabilized β-phase fraction at room temperature than Ti–6Al–4V alloy [18]. As a near-β alloy, Ti6246 usually forms a β-phase matrix with stable primary α-phase grains [9]. When the alloy is aged, secondary α-phase particles also evolve in the β-phase matrix. For industrial applications, Ti6246 is primarily processed via the forging route [19,20].

To the best of our knowledge, although the Ti6246 alloy is well established, studies on the prospect of processing Ti6246 using LPBF technology are limited [18,21–23]. Numerous studies have shown that β-forged Ti6246 increases the retained β-phase fraction, leading to impressive properties such as high low-cycle fatigue, fatigue crack growth resistance, high fracture toughness, and an increase in service temperature without decreasing thermal stability [20,24,25]. The LPBF process involves higher cooling rates ($\sim 10^8$ K/s) than that of the β-forging of Ti6246 [26], which in theory suggests that more β phase should freeze or be retained in the processing of Ti6246 than in the forging process. Therefore, in this study, we investigated the LPBF processability of Ti6246. This study exploits a wide LPBF process parameter window to evaluate the correlation between the process parameters and Ti6246 microstructure evolution. Moreover, the hardness properties of the microstructures generated from different process parameters were investigated. Single-scan laser irradiation experiments and computational thermal fluid dynamics (CtFD) simulations of selected processing conditions provided further insights into the melting and solidification modes. Overall, this study aimed to further enrich the available knowledge on LPBF processing of Ti alloys by filling the knowledge gap involving β-stabilized α+β alloys, in particular, Ti6246.

2. Material and methods

2.1. LPBF processing of samples

Ti6246 alloy ingots were Ar gas-atomized to produce starting powders for the LPBF process. The powder particles showed almost spherical morphologies (Fig. 1) with a particle size distribution of D_{10} = 24.7, D_{50} = 38.5, and D_{90} = 61.5 μm, measured using a particle size analyzer
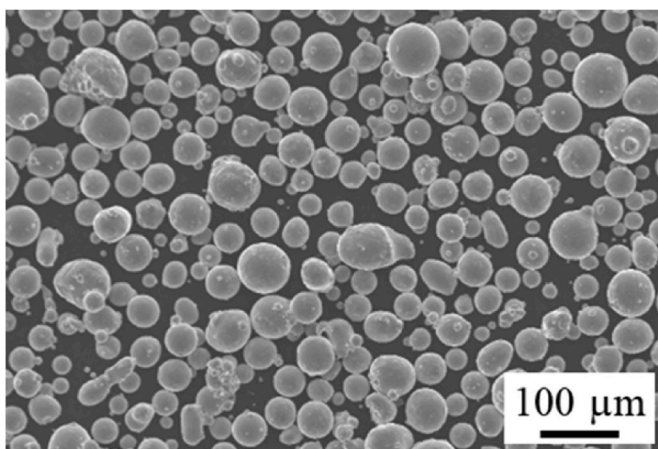

Fig. 1. SEM image of the gas-atomized Ti6246 starting powder.

(Mastersizer 3000E, Malvern Panalytical, UK). Table 1 summarizes the chemical composition of the Ti6246 powder.

Using the LPBF equipment (EOS M290, EOS GmbH, Germany), bulk cylindrical samples with a diameter of 7 mm and height of 10 mm were fabricated (Fig. 2). The building chamber was filled with high-purity Ar gas to maintain the oxygen content below 100 ppm. The process parameters for the fabrication of the specimens included a fixed hatch spacing d and layer thickness t of 100 and 60 μm, respectively. The laser power P and laser scan speed v were varied within the ranges of 180–360 W and 600–1400 mm/s, respectively. The energy inputs involved in the build were quantified as volumetric energy density (VED), defined as

$$\text{VED} \ (\text{J} / \text{mm}^3) = \frac{P}{vdt}. \tag{1}$$

The production conditions are listed in Table 2. To better understand the effects of the LPBF process parameters on the phase and microstructure evolution, the fabricated samples were grouped according to their VEDs (Fig. 2(a)). A bidirectional scan strategy was used along the X-axis with no rotations in the subsequent layers (Fig. 2(b)). The build direction was defined as the Z direction, and the direction perpendicular to the X- and Z-directions was defined as the Y direction. Under all fabrication conditions, cylindrical samples without any apparent defects were produced (Fig. 2(c)).

2.2. Phase identification by X-ray diffraction

X-ray diffraction (XRD) analysis was performed on the as-built samples (SmartLab, Rigaku, Japan) using a Cu-Kα radiation source operating at 40 kV and 30 mA. Scanning was performed from 10 to 90° (2θ) at a scan rate of 2°/min.

2.3. Microstructural observation

To investigate the effects of the LPBF process parameters on the microstructural evolution, the fabricated samples were sectioned and mounted to observe the YZ plane (Fig. 2(b)). The samples were mechanically ground and polished to 3 μm using the appropriate diamond suspensions and then chemically polished to a mirror finish using a colloidal silica suspension. A scanning electron microscope (SEM; JSM-7200F, JEOL, Japan) equipped with an electron backscatter diffractometer (EBSD) was used to characterize the microstructures. Observations were performed in a region 1–2 mm from the top edge of the sample in the YZ plane (green region in Fig. 2(b)).

2.4. Hardness test

Microhardness tests were conducted using a Vickers microhardness tester (HMV-G31; Shimadzu, Japan) with a load of 300 gf (~ 2.94 N) and dwell time of 5 s. Twenty random indentations were made in the previously defined region of the YZ plane (green region in Fig. 2(b)) for each sample. The average and standard deviation of the indentations are noted.

2.5. CtFD simulations

CtFD simulations of laser beam irradiation were performed using a commercial 3D thermo-fluid analysis software (Flow-3D® with Flow-3D Weld module, Flow Science, USA) to investigate the solidification behavior under LPBF processing depending on the manufacturing

Table 1
Chemical composition of Ti6246 powder.

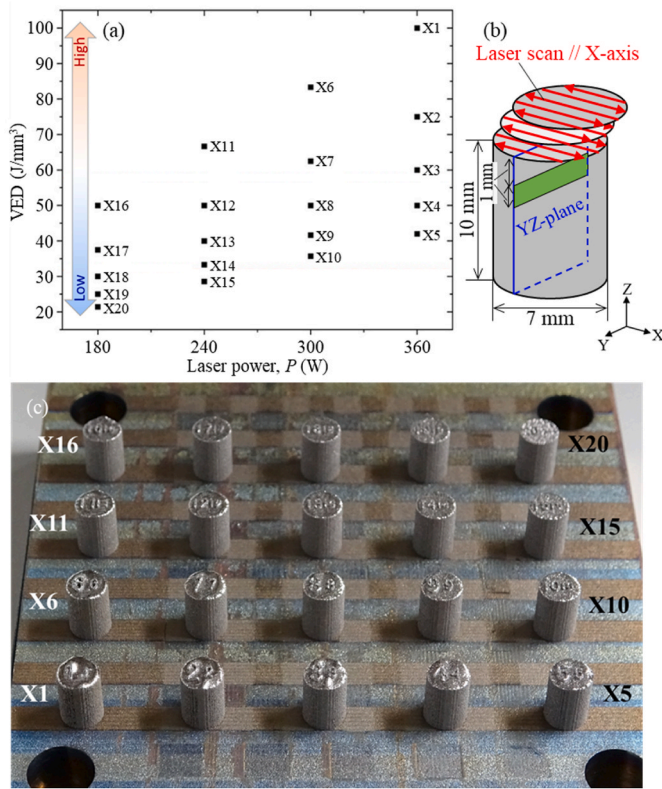| Chemical element	Ti	Al	Sn	Zr	Mo
Quantity (mass%)	Balance	4.67	2.17	3.79	5.14

Fig. 2. (a) Summary of laser conditions with respect to VED. (b) Shape and geometry of the fabricated sample and laser scan strategy adopted in this study. Microstructural observations and hardness tests were performed within the green-hatched region. (c) Photograph of the fabricated samples.

Table 2
LPBF process parameters used in this study.

Sample name	Process parameters				
	Laser power P (W)	Scan speed v (mm/s)	Hatch distance d (μm)	Layer thickness t (μm)	VED (J/mm³)
X1	360	600	100	60	100.00
X2		800			75.00
X3		1000			60.00
X4		1200			50.00
X5		1400			42.86
X6	300	600			83.33
X7		800			62.50
X8		1000			50.00
X9		1200			41.67
X10		1400			35.71
X11	240	600			66.67
X12		800			50.00
X13		1000			40.00
X14		1200			33.33
X15		1400			28.57
X16	180	600			50.00
X17		800			37.50
X18		1000			30.00
X19		1200			25.00
X20		1400			21.43

parameters.

The laser heat sources were modeled using a Gaussian distribution, in which the irradiation intensity distribution of the beam was regarded as a symmetrical Gaussian distribution over the entire beam. The beam intensity distribution $\dot{q}$ is expressed as follows:

$$\dot{q} = \frac{2\eta P}{\pi r_0^2} \exp\left(-\frac{2r^2}{r_0^2}\right), \tag{2}$$

where P is the beam power, r_0 is the effective beam radius, r is the actual beam radius, and η is the beam absorption rate. To increase the accuracy of the model, we calculated η by assuming multiple reflections using the Fresnel equation:

$$\eta = 1 - \frac{1}{2}\left\{\frac{1 + (1 - \varepsilon \cos \theta)^2}{1 + (1 + \varepsilon \cos \theta)^2} + \frac{\varepsilon^2 - 2\varepsilon \cos \theta + 2 \cos^2 \theta}{\varepsilon^2 + 2\varepsilon \cos \theta + 2 \cos^2 \theta}\right\}, \tag{3}$$

where ε is the Fresnel coefficient, and θ is the incident angle of the laser. The fitting parameter ε was validated by optimizing this value to match the experimentally obtained melt pool shape [27,28]. Local melting causes material vaporization and leads to high vapor pressure. This vapor pressure acts as recoil pressure on the surface, pushing the melt pool down. The recoil pressure was reproduced using the following model:

$$p_{\text{recoil}} = Ap_0 \exp\left[\frac{\Delta H_{\text{LV}}}{RT_{\text{V}}}\left(1 - \frac{T_{\text{V}}}{T}\right)\right], \tag{4}$$

where p_0 is the atmospheric pressure, ΔH_{LV} is the latent heat of vaporization, R is the gas constant, T_{V} is the boiling point at the saturated vapor pressure, and A is a ratio coefficient that is generally assumed to be 0.54, indicating that the recoil pressure due to evaporation is 54% of the vapor pressure at equilibrium on the liquid surface.

Table 3 lists the simulation parameters, most of which were evaluated using alloy physical property calculation software (JMatPro v11, Sente software, UK). Density, viscosity, specific heat, thermal conductivity, surface tension, and compressibility were used, and the temperature dependences are shown in Supplementary Fig. 1S. The emissivity and Stefan–Boltzmann constant values were obtained from the literature [29], and the values for pure Ti [30] were used for the heat of vaporization and the vaporization temperature. The dimensions of the computational domain of the numerical model were 11.0 mm in the beam scanning direction, 0.4 mm width, and 0.8 mm height. A uniform mesh size of 10 μm is applied to the computational domain. The boundary condition of continuity was applied to all the boundaries, except for the top surface. The temperature was initially set to 300 K and P and v were the same as those used in the experiments. The fitting parameter ε was used to reproduce the experimentally obtained melt pool shape. The solidification conditions at the solid–liquid interface, that is, temperature gradient G, solidification rate R, and cooling rate $\dot{T}$, where $\dot{T} = G \times R$, were calculated from the obtained temperature distributions. The validity of the calculation was verified by comparing the calculated melt-pool shape with that generated experimentally by laser scanning. For this purpose, the laser was scanned on a bulk Ti6246 sample under the same conditions as those used for fabrication, and the

Table 3
Physical parameters used in CtFD simulations.

Property	Symbol	Value
Density at 300 K	ρ	4.645 g/cm³ [a]
Liquidus temperature	T_{L}	1980 K [a]
Solidus temperature	T_{S}	1938 K [a]
Viscosity at T_{L}	μ	3.49 g/m/s [a]
Specific heat at 300 K	C_{P}	0.519 J/g/K [a]
Thermal conductivity at 300 K	λ	6.00 W/m/K [a]
Surface tension at T_{L}	γ_{L}	1.638 J/m² [a]
Compressibility at 300 K	κ	9.19×10^{-3} 1/GPa [a]
Emissivity	E	0.27 [31]
Stefan–Boltzmann constant	σ	5.67×10^{-8} W/m²/K⁴ [29]
Heat of vaporization	ΔH_{LV}	425.8 kJ/mol [30]
Vaporization temperature	T_{V}	3558.15 K [30]

[a] Calculated using JMatPro v11.

melt-pool shape was observed.

3. Results

3.1. Phase identification

The XRD analysis revealed that the starting powder primarily consisted of hcp and bcc β phases, with an unidentified peak observed at approximately 41° (Fig. 3). No peaks corresponding to the ω phase were observed. For the Ti6246 samples produced by LPBF, the XRD patterns match the characteristic peaks associated with the Ti6246 alloy [31,32]. Considering the high cooling rate during LPBF, it is generally reasonable to assume that the hcp phase in the fabricated Ti6246 samples is the martensitic α' phase [32]. However, because the α and α' phases have the same hcp structure and are usually indistinguishable based on the XRD peak positions, the peak attributed to this hcp phase is described as α/α'. Additionally, we observed an increase in the peak intensity of the β phase with an increase in VED, as indicated by the (200) peak.

3.2. Effect of LPBF process parameters on phase and microstructure evolution

Fig. 4 depicts typical inverse pole figure (IPF) maps obtained in the YZ plane. Ti6246 solidified with the bcc β phase and transformed into the hcp α/α' phase in accordance with the Burgers orientation relationship. The IPF maps in Fig. 4 represent the orientation distribution of the bcc phase, which was back-transformed from the hcp phase according to the Burgers relationship. In other words, these IPF maps show the β grain structure during solidification before the β → α/α' phase transformation occurs.

The samples fabricated under high VEDs with combinations of relatively high P and low v (e.g., X1–X3, X6, X7, and X11) formed pronounced columnar microstructures along the build direction. A columnar microstructure along the build direction is a characteristic feature of products fabricated using the scan strategy without the rotation of the laser scan direction [5,33]. The columnar microstructure results from epitaxial growth between the layers [5,33], and, as a corollary, the grain size along the build direction significantly exceeds the layer thickness (60 μm). The samples fabricated with intermediate VEDs exhibited columnar microstructures similar to those produced with high VEDs, although they were relatively less distinct. In contrast, the samples fabricated under low VEDs with a relatively low laser power and high scan speed (e.g., X15 and X18–X20) showed polycrystalline
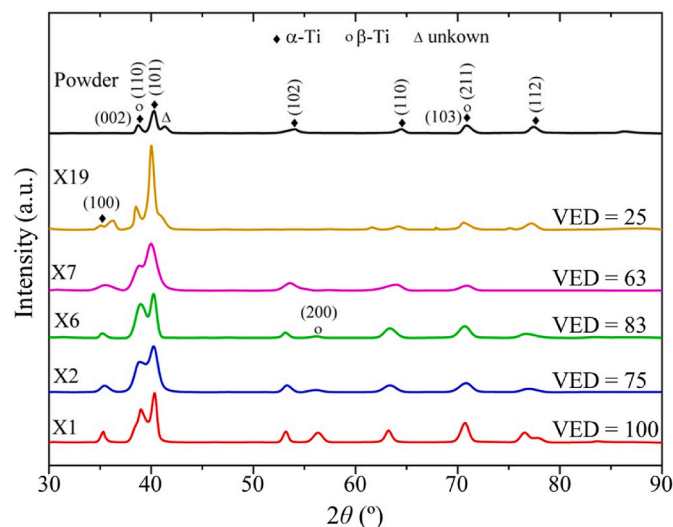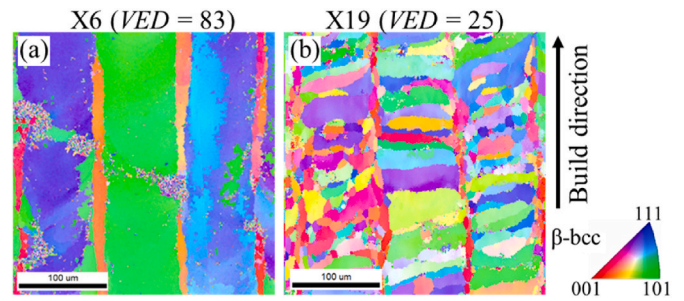

Fig. 4. IPF map of the β phase, taken in the YZ-plane, showing the β-solidifying grain structure for (a) sample X6 fabricated under high VED (300 W, 600 mm/s) with a columnar microstructure and (b) sample X19 fabricated under low VED (180 W, 1200 mm/s) with a polycrystalline microstructure.

microstructures with smaller grains.

Fig. 5(a) shows the SEM microstructure of the specimens consisting of the β and α/α' phases observed in the YZ plane. The α/α' phases appear as black areas in the SEM micrographs (Fig. 5(a)). The high-VED samples, X1–X3, X6, X7, and X11, exhibited extremely refined microstructural features with nanosized acicular α/α' phases, as shown in Fig. 5(b). In the low-VED samples (X15 and X18–X20), relatively coarse microsized acicular α/α' grains were formed over the entire sample (Fig. 5(d)). For the intermediate-VED samples, the size of the acicular α/α' grains was intermediate between that of the high- and low-VED samples (Fig. 5(c)). The higher the VED, the greater the tendency to form a finer acicular microstructure.

3.3. Variation in hardness

The hardness of the Ti6246 samples fabricated via LPBF ranged from 513 ± 23 HV (sample X6) to 329 ± 13 HV (sample X20). Most of the samples demonstrated higher hardness than the β-forged Ti6246 reference sample (384 ± 26 HV). The hardness of the samples at each laser power decreased with increasing scanning speed, and at each laser scan speed, the hardness decreased with decreasing laser power (Fig. 6(a)). From another perspective, the hardness increases as the VED increases (Fig. 6(b)). The positive correlation between hardness and VED is attributed to microstructural refinement because the size of the α/α' phase was significantly larger at low VED, as shown in Fig. 5. However, on the high-VED side, the effect of the VED gradually decreases (the slope of the graph decreases, as indicated by the blue enclosure), and sample X1 completely deviated from this trend.

3.4. CtFD simulation results

Fig. 7(a) shows an example snapshot of the CtFD simulation under the laser conditions of P = 300 W and v = 600 mm/s (X6). A melt pool with an elongated teardrop shape was formed. CtFD simulations were performed with various Fresnel coefficients, which correlated to the beam absorption efficiency, and the Fresnel coefficient was determined to reproduce the experimentally obtained melt pool shape [27,28]. Fig. 7(b) and (c) compare the size of the melt pool generated via single-scan track experiments and CtFD simulations to validate the simulation outcomes. In the simulation results, the red area represents the region that has fully melted once during laser scanning, and the blue area represents the region that has not even partially melted. The size and shape of the melt pool observed in the simulations were in good agreement with the respective single-scan track experiments for both high- and low-VED fabrication conditions.

CtFD simulations with various P and v conditions corresponding to the LPBF fabrication were performed to estimate the temperature gradient G and solidification rate R at the liquid-solid interfaces. The G and R values at the moment of solidification of each site in the melt pool

Fig. 3. XRD patterns of the starting powder and selected Ti6246 samples produced by LPBF using various VEDs in the YZ plane.
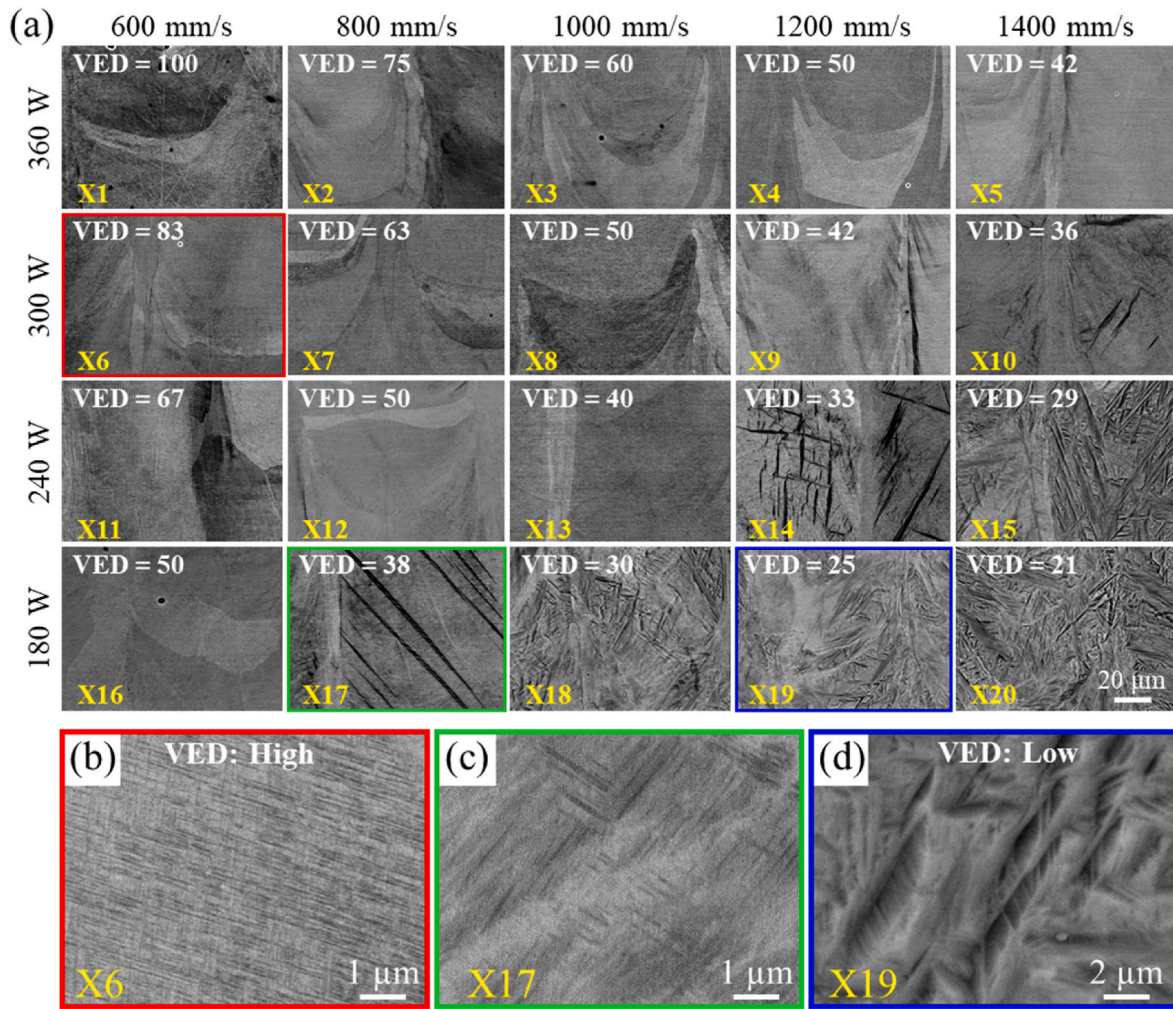
Fig. 5. (a) SEM micrographs of Ti6246 samples fabricated via LPBF under different processing conditions with various VEDs and magnified SEM images of samples fabricated with (b) high VED (X6), (c) intermediate VED (X17), and (d) low VED (X19).

under all fabrication conditions are shown on the solidification (G–R) map (Fig. 8). To output the temperature conditions at the solid-liquid interface in the melt pool, only the data for each mesh with a solid-phase fraction of approximately 0.5 in the CtFD simulation was evaluated. There was a clear tendency for the solidification behavior to transition toward a high G and high R as the VED decreased. Multiple regression analysis revealed that the laser power P had a negative effect on G and R, and thus on the cooling rate $\dot{T}$, whereas the scanning speed v had a positive effect (Table 4). Thus, $\dot{T}$, defined as $G \times R$, becomes larger with smaller P and larger v. According to the standard partial regression coefficients β and p-values, P had a relatively large effect on R and v on G. Although it has been reported in studies under constant P conditions that $\dot{T}$ increases with increasing v [34], this is the first study to clarify the comprehensive effects of P and v on G, R, and $\dot{T}$ over a wide range of P and v conditions.

Fig. 9 shows the simulated temperature change in the pre-solidified part immediately beneath the melt pool as a result of laser irradiation (scanning). The temperature changes at the melt pool bottom (0 μm) and at 30 and 60 μm below the bottom under high-VED conditions (300 W and 600 mm/s, consistent with X6 conditions) and, for comparison, under low-VED conditions (180 W and 1200 mm/s, consistent with X19 conditions) are shown in the figure. The depth of 60 μm corresponds to the layer thickness. Near the melt pool bottom, the maximum temperature reached was higher, and steep heating and cooling occurred.

Below the melt pool bottom, the temperature change slowed and the maximum temperature decreased.

4. Discussion

The hardness of Ti6246 fabricated via LPBF with various fabrication parameters depended on the size of the α/α' phase, with a finer α/α' phase showing higher strength owing to the interphase strengthening effect (except for the X1 sample fabricated with the highest VED). Furthermore, the size of the α/α' phase became finer with a higher VED.

4.1. Reasons for α/α' grain refinement as VED increases

Possible factors affecting the size of the α/α' phase are the primary β grain size and density of the α' martensite nucleation sites [35]. Smaller β grains result in finer α' martensite grains [36]. However, in the present study, coarse α/α' grains appeared when the β grain size was small, indicating that the primary β grain size was not a determinant of the α/α' phase size.

The microstructure of the primary β-grains tended to change significantly depending on the VED (Fig. 4). Columnar microstructures along the build direction evolved under high VED conditions, whereas polycrystalline microstructures with smaller grain sizes were obtained under low VED conditions. Under a high VED, the length of the β grains was considerably longer than the layer thickness (60 μm), suggesting that
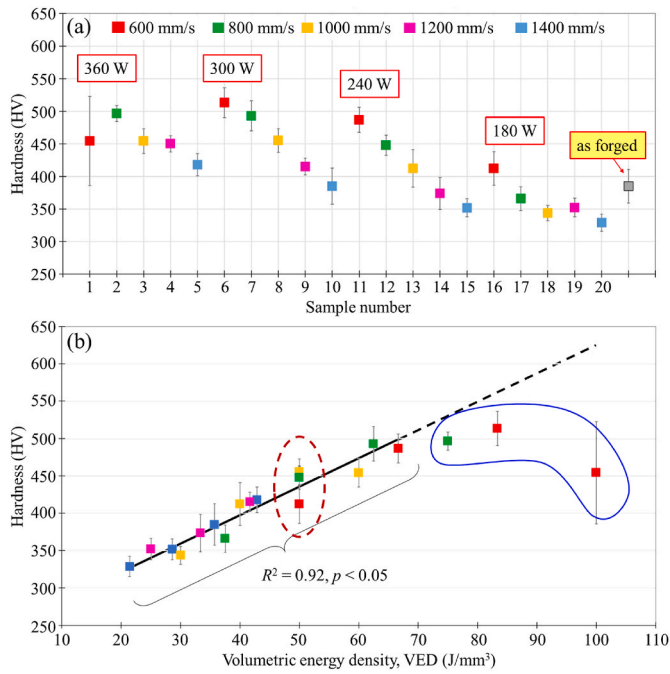
Fig. 6. Hardness of Ti6246 samples fabricated via LPBF as a function of (a) laser power P and scan speed v and (b) VED. The red dashed oval refers to the samples produced with the same VED of 50 J/mm^3 (see Section 4.3). The R^2 and p-values were calculated using the data for VED <70 J/mm^3.

epitaxial growth was dominant. The characteristic alternating stacking of thick and thin layers is shown (Fig. 4(a)). This thin layer occurs at the central bottom of the melt pool and is formed by the preferential growth of the <100>, the easy growth direction of the cubic crystal, along the build direction owing to the downward heat flow [5], which is the first report of such an occurrence in bcc alloys. Thijs et al. [37] elucidated that the bidirectional X-scan strategy with no rotations in layers assists columnar microstructure formation because the laser trajectories remain the same in each layer. Consequently, the thermal flux was homogenous for every layer, thereby facilitating epitaxial growth. This is true when fabricating under high VED conditions but does not hold outside a certain VED range, as shown in this study.

The size of the primary β phase decreased with increasing cooling rate $\dot{T}$, that is, with decreasing VED. This is consistent with the trend observed in Ni-based [38] and β-Ti alloys [39], which do not undergo solid-solid phase transformations during fabrication. In rapid solidification, the following relationship between grain size D and $\dot{T}$ has been reported [40]:

$$D = \alpha \bullet \dot{T}^{-n}, \tag{5}$$

where α and n are material-specific constants.

The increase in $\dot{T}$ sometimes causes a transition in the solidification

behavior (G–R) from a region of planar growth (high G/R) to that of dendritic growth (low G/R), located on the opposite side of the columnar-to-equiaxed transition (CET) line. The value of G/R represents constitutional supercooling and correlates with crystalline formation [41]. A lower G/R ratio indicates that compositional undercooling is more likely to result in a possible loss of the smooth solid–liquid interface. Consequently, nucleation may result in the formation of equiaxed grains and unstable dendrites [42], producing a more random texture. However, the solidification behavior revealed in the present study is that as VED decreases, $\dot{T}$ increases from 7.7×10^5 to 4.9×10^6 while G/R remains almost constant. This suggests that the polycrystal formation is not due to compositional undercooling. Therefore, the reduction of β-grain size would be responsible for the deviation of the melt pool shape and the related heat flow directionality from the ideal situation for epitaxial crystal growth over multiple melt pools [6].

Fig. 8. Solidification (G–R) map representing the effect of the LPBF fabrication condition (VED) on thermal gradient G and solidification rate R. Light blue markers indicate the conditions with VED = 50 J/mm^3 (see Section 4.3).

Table 4
Multiple regression analysis representing the effects of P and v on G and R.

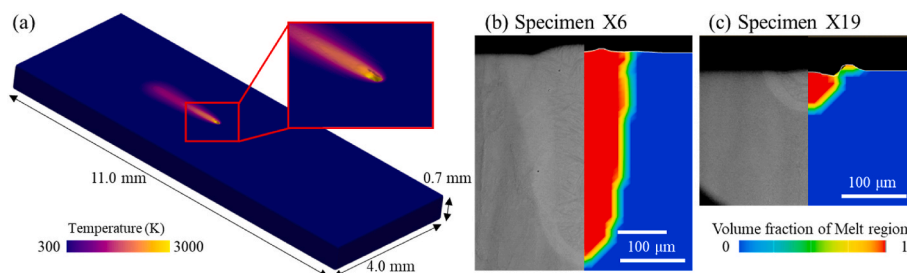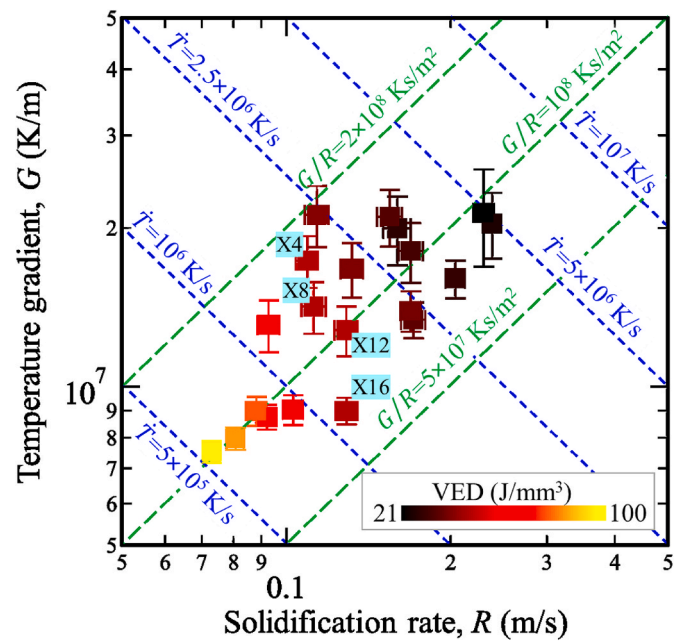|	R^2	P		v	
		β	p-value	β	p-value
G	0.96	−0.19	7.0×10^{-4}	0.96	1.7×10^{-13}
R	0.88	−0.77	2.8×10^{-8}	0.54	3.2×10^{-6}

Fig. 7. (a) Snapshot of the CtFD simulation of laser-beam irradiation on the Ti alloy. Comparison between melt pool size after single-scan track experiment and CtFD simulation to validate the simulation outcome. (b) Specimen X6 (300 W, 600 mm/s) and (c) specimen X19 (180 W, 1200 mm/s).
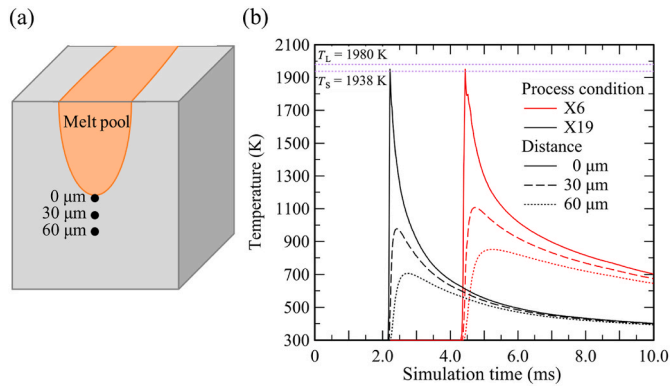
Fig. 9. (a) Locations where the temperature change was analyzed and (b) temperature change during laser scanning under X6 (300 W, 600 mm/s) and X19 (180 W, 1200 mm/s) conditions.

Another possibility is the density of α' martensite nucleation sites. It has been documented that the density of α' martensite nucleation sites increases with increasing input laser energy density during LPBF, resulting in refined α' martensite grains [43]. Dislocations are considered to be the preferred nucleation sites for martensite. Products manufactured by LPBF contain large amounts of dislocations [44], indicating abundant nucleation sites. The available nucleation site density N_0 can be estimated as a function of the irradiated laser intensity as follows [45].

$$N_0 = \frac{1}{2}\rho_{\text{dis}}(I, T)^{1.5},\tag{6}$$

where ρ_{dis} is the dislocation density, I is the laser intensity, and T is the temperature. A higher laser intensity activated the nucleation sites, leading to the formation of finer α'-grains.

4.2. Reason for the decreasing trend of hardness at higher VED

At a higher VED, a decreasing trend in hardness was observed despite the finer α/α' phase size. To discuss this unusual trend, the thermal effect of laser irradiation on the pre-solidified part just beneath the melt pool must be considered rather than the solidification behavior in the melt pool.

From the XRD peak profiles, the higher the VED, the sharper the hcp peaks and the higher the bcc peak intensity, which implies the decomposition of α' martensite into α and β phases. The α phase and α' martensite both have hcp structures; therefore, they exhibit very similar XRD peak patterns. However, α' martensite can be distinguished from the α phase because its peak width is broader [46] owing to its higher level of dislocations, and thus, lattice distortion caused by rapid cooling [47]. Sharpening of the peak at a high VED suggests that the dislocation density decreased and the α' structure approached the α structure. This leads to a decrease in strength [48].

The simulated temperature changes in the pre-solidified part beneath the melt pool shown in Fig. 9 indicate the possibility of heat-treatment-like thermal effects on the pre-solidified layer underneath. Under high-VED conditions, the retention time at elevated temperatures was significantly longer. The decomposition of martensite has been reported to occur at retention temperatures of 550–650 °C (823–923 K) [32,49]. Martensite formed in LPBF decomposes in much less than 1 min for heat treatment at 650 °C [22]. The samples fabricated under relatively high-VED conditions would be more strongly affected by thermal effects owing to the longer exposure to high temperatures. The effect of such steep heating and cooling on the phase transformation, as can occur in the LPBF process, has not yet been well demonstrated and should be examined in the future.

4.3. Variations in solidification and reheating behavior and resultant hardness despite equal VED

In this study, we used the VED to explain the major trends (e.g., Vickers hardness in Fig. 6). VED is the standard index of manufacturing conditions used to control the properties and quality of products manufactured using the PBF method [50]. The VED is composed of a combination of the laser power, laser scan speed, hatch spacing, and layer thickness; it does not reflect the balance of each of these condition elements. In this study, the VED of samples X4, X8, X12, and X16 were equal to 50 J/mm³. Nevertheless, with respect to hardness, X16 (shown in red), which was fabricated with the lowest laser power and slowest scanning speed, exhibited a lower hardness than the others (see dashed ellipses in Fig. 6). The differences in fabrication conditions affected the solidification behavior in the melt pool (Fig. 8) and the reheating conditions beneath the melt pool (Fig. 10). In particular, the fabrication condition for sample X16 (lowest hardness) tended to induce a smaller thermal gradient during solidification and a longer retention time at high temperatures during reheating than the other three conditions. That is, among the four conditions with VED = 50 J/mm³, the X16 condition exhibited solidification behavior and hardness closer to that of the high-VED condition described in Section 4.2.

This suggests that in LPBF, VED broadly reflects but is not necessarily a univocal indicator of product characteristics, and that product properties can vary with the balance of condition elements composing the VED. This finding provides important insight into the need to consider not only the VED but also various conditions individually for more precise control of product properties.

4.4. Limitations

This study has several limitations. The volume fraction of the β phase and the dislocation density, which affect the hardness, have not been quantified. The volume fraction of the phase can be quantified by EBSD and XRD; however, in this study, the very fine microstructure (Fig. 5 (b–d)) and the fabrication condition-dependent development of different crystallographic textures in LPBF [51], respectively, were obstacles to reliable quantification. Dislocation density is analyzed using XRD, TEM, and EBSD, however, the absence of elastic modulus in each crystallographic direction of this alloy, the very localized field of view in TEM for possible heterogeneities described below, and the very fine
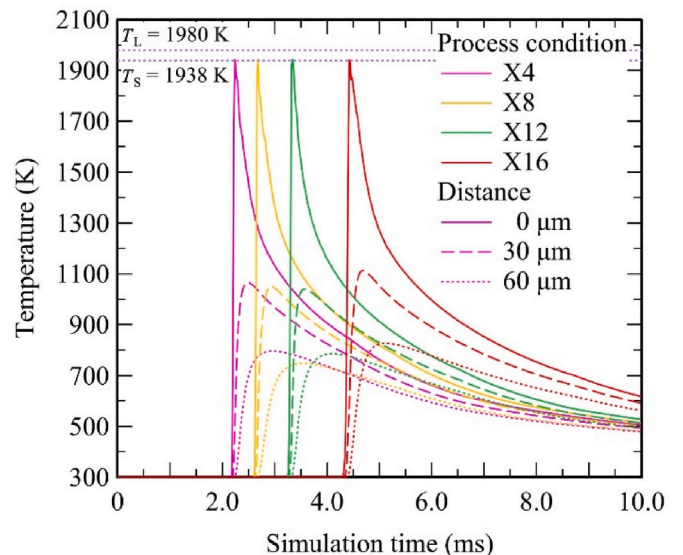

Fig. 10. Temperature change during laser scanning under X4, X8, X12, and X16 conditions with VED = 50 J/mm³.

microstructure, respectively, hindered quantification. In addition, the large variation in hardness in sample X1 (Fig. 6), produced under the highest VED conditions, suggested heterogeneities in the microstructure and hardness; however, no analysis was performed assuming heterogeneity in this study.

4.5. Future prospective

In powder bed fusion (PBF) methods, the anisotropy of physical and/or chemical properties due to anisotropic grain morphology and crystallographic textures is sometimes a problem. A fixed manufacturing direction is responsible for this challenge. Because the temperature gradient G is extremely large in LPBF, it is extremely difficult to obtain an equiaxed microstructure by achieving compositional undercooling by adjusting the solidification conditions (G, R, $\dot{T}$, and G/R) [52].

Equiaxed polycrystallisation can be achieved using inclusions or particle inoculants as heterogeneous nucleation sites in the liquid phase [53,54]. Another promising strategy is the use of solid-phase transformations. In particular, an isotropic microstructure can be obtained when there are a number of equivalent variant relationships, such as the Burgers orientation relationship seen in the transformation from the bcc to the hcp phase in Ti alloys. Furthermore, as shown in this study, the α/α' phase size after the phase transformation could be largely varied independently of the microstructural feature size of the primary phase to obtain the desired mechanical properties.

However, if metastable phases such as martensite are formed by rapid cooling, thermal effects in the pre-solidified part just beneath the melt pool must be considered. For example, the transformation from the α' phase to the α phase reduces strength. In another example, thermal effects can precipitate α [55] and ω [56] phases in the metastable β phase, which is obtained by rapid cooling, and deteriorate the performance of the biomaterial by increasing Young's modulus.

The successful use of the thermal effects could enable precipitation of the strengthening phases in situ. Thus, in the LPBF process, the functionality of the alloys can be controlled through thermal effects on the solidified part below the melt pool, depending on the alloy type. Furthermore, as shown in Figs. 9 and 10, the degree of reheating depends on the distance from the bottom of the melt pool. In other words, by introducing heterogeneity in the microstructure and mechanical properties, that is, hard and soft domains, hetero-deformation-induced hardening may lead to the acquisition of materials with superior mechanical properties [57]. This study demonstrates this possibility.

5. Conclusions

In this study, we fabricated a Ti6246 alloy under a wide range of manufacturing conditions using LPBF and comprehensively analyzed variations in phase, microstructure, and hardness and their causes using numerical analysis. The following conclusions were drawn:

- Hardness showed a significant positive correlation with the VED of the laser in the range of VED <70 J/mm^3; a decreasing trend in hardness was observed for fabrication conditions with VED >70 J/mm^3.
- The microstructure of the primary β phase is highly oriented under high-VED conditions and polycrystalline under low-VED conditions, which is consistent with previously reported trends. In contrast, the α/α' microstructure after the phase transformation shows an opposite trend to the β microstructure with respect to the VED, becoming extremely fine under high-VED conditions.
- The thermal effects on the pre-solidified parts (reheating effect) were more pronounced under high VED conditions. Numerical calculations show that the duration of exposure of the pre-solidified parts to high temperatures is prolonged under high VED conditions.

- As a result of the reheating effect, α' martensite with a high dislocation density partially decomposed into α and β phases under high-VED conditions, which is detectable by XRD profiles. Owing to the phase transformation, samples manufactured under high-VED conditions show a degradation of hardness.

In conclusion, a combination of duplicate LPBF-specific thermal histories, rapid cooling, and reheating of the pre-solidified part determines the final mechanical properties via metastable α' phase evolution and partial phase decomposition into $\alpha + \beta$ phases.

CRediT authorship contribution statement

Prince Valentine Cobbinah: Conceptualization, Investigation, Writing - original draft, Formal analysis, Visualization, Writing - review & editing. Sae Matsunaga: Writing - review & editing, Visualization. Yoshiaki Toda: Conceptualization, Funding acquisition, Writing - review & editing. Ryosuke Ozasa: Resources, Investigation, Formal analysis, Writing - review & editing. Masayuki Okugawa: Resources, Investigation, Formal analysis, Validation, Writing - review & editing. Takuya Ishimoto: Resources, Investigation, Writing - original draft, Formal analysis, Writing - review & editing, Visualization. Yuhen Liu: Resources, Investigation, Formal analysis, Validation, Writing - review & editing. Yuichiro Koizumi: Resources, Investigation, Formal analysis, Validation, Visualization, Writing - review & editing. Pan Wang: Validation, Writing - review & editing. Takayoshi Nakano: Resources, Investigation, Funding acquisition, Formal analysis, Validation, Writing - review & editing. Yoko Yamabe-Mitarai: Conceptualization, Funding acquisition, Formal analysis, Resources, Validation, Writing - review & editing, Visualization, Supervision.

Data availability

The data will be made available upon request.

Declaration of competing interest

The authors declare the following financial interests/personal relationships which may be considered as potential competing interests: Pan Wang is one of Editorial Board Members of Smart Materials in Manufacturing. If there are other authors, they declare that they have no known competing financial interests or personal relationships that could have appeared to influence the work reported in this paper.

Appendix A. Supplementary data

Supplementary data to this article can be found online at https://doi.org/10.1016/j.smmf.2024.100050.

References

[1] B. Blakey-Milner, P. Gradl, G. Snedden, M. Brooks, J. Pitot, E. Lopez, M. Leary, F. Berto, A. du Plessis, Metal additive manufacturing in aerospace: a review, Mater. Des. 209 (2021) 110008, https://doi.org/10.1016/j.matdes.2021.110008.

[2] M. Khorasani, A. Ghasemi, B. Rolfe, I. Gibson, Additive manufacturing a powerful tool for the aerospace industry, Rapid Prototyp. J. 28 (2022) 87–100, https://doi.org/10.1108/RPJ-01-2021-0009.

[3] H. Attar, S. Ehtemam-Haghighi, D. Kent, M.S. Dargusch, Recent developments and opportunities in additive manufacturing of titanium-based matrix composites: a review, Int. J. Mach. Tool Manufact. 133 (2018) 85–102, https://doi.org/10.1016/j.ijmachtools.2018.06.003.

[4] Y. Liu, K. Nose, M. Okugawa, Y. Koizumi, T. Nakano, Fabrication and process monitoring of 316L stainless steel by laser powder bed fusion with μ-helix scanning strategy and narrow scanning line intervals, Mater. Trans. 64 (2023) 1135–1142, https://doi.org/10.2320/matertrans.mt-me2022006.

[5] O. Gokcekaya, T. Ishimoto, S. Hibino, J. Yasutomi, T. Narushima, T. Nakano, Unique crystallographic texture formation in Inconel 718 by laser powder bed fusion and its effect on mechanical anisotropy, Acta Mater. 212 (2021) 116876, https://doi.org/10.1016/j.actamat.2021.116876.

[6] K. Hagihara, T. Nakano, Control of anisotropic crystallographic texture in powder bed fusion additive manufacturing of metals and ceramics–A review, JOM 74 (2022) 1760–1773, https://doi.org/10.1007/s11837-021-04966-7.

[7] N. Soro, E.G. Brodie, A. Abdal-hay, A.Q. Alali, D. Kent, M.S. Dargusch, Additive manufacturing of biomimetic titanium-aantalum lattices for biomedical implant applications, Mater. Des. 218 (2022) 110688, https://doi.org/10.1016/j.matdes.2022.110688.

[8] J.C. Williams, R.R. Boyer, Opportunities and issues in the application of titanium alloys for aerospace components, Metals 10 (2020) 705, https://doi.org/10.3390/met10060705.

[9] R.P. Kolli, A. Devaraj, A review of metastable beta titanium alloys, Metals 8 (2018) 506, https://doi.org/10.3390/met8070506.

[10] T. Ishimoto, K. Hagihara, K. Hisamoto, S.-H. Sun, T. Nakano, Crystallographic texture control of beta-type Ti–15Mo–5Zr–3Al alloy by selective laser melting for the development of novel implants with a biocompatible low Young's modulus, Scripta Mater. 132 (2017) 34–38, https://doi.org/10.1016/j.scriptamat.2016.12.038.

[11] T. Nagase, T. Hori, M. Todai, S.-H. Sun, T. Nakano, Additive manufacturing of dense components in beta-titanium alloys with crystallographic texture from a mixture of pure metallic element powders, Mater. Des. 173 (2019) 107771, https://doi.org/10.1016/j.matdes.2019.107771.

[12] D. Gu, Y.C. Hagedorn, W. Meiners, G. Meng, R.J.S. Batista, K. Wissenbach, R. Poprawe, Densification behavior, microstructure evolution, and wear performance of selective laser melting processed commercially pure titanium, Acta Mater. 60 (2012) 3849–3860, https://doi.org/10.1016/j.actamat.2012.04.006.

[13] Y.P. Dong, Y.C. Tang, D.W. Wang, N. Wang, Z.D. He, J. Li, D.P. Zhao, M. Yan, Additive manufacturing of pure Ti with superior mechanical performance, low cost, and biocompatibility for potential replacement of Ti-6Al-4V, Mater. Des. 196 (2020) 109142, https://doi.org/10.1016/j.matdes.2020.109142.

[14] H. Amano, T. Ishimoto, R. Suganuma K. Aiba, S.-H. Sun, R. Ozasa, T. Nakano, Effect of a helium gas atmosphere on the mechanical properties of Ti-6Al-4V alloy built with laser powder bed fusion: a comparative study with argon gas, Addit. Manuf. 48 (2021) 102444, https://doi.org/10.1016/j.addma.2021.102444.

[15] Z. Li, K. Ming, B. Li, S. He, B. Miao, S. Zheng, Optimizing strength-ductility of laser powder bed fusion-fabricated Ti–6Al–4V via twinning and phase transformation dominated interface engineering, Mater. Sci. Eng., A 882 (2023) 145484, https://doi.org/10.1016/j.msea.2023.145484.

[16] Z. Yao, X. Jia, J. Yu, M. Yang, C. Huang, Z. Yang, C. Wang, T. Yang, S. Wang, R. Shi, J. Wei, X. Liu, Rapid accomplishment of strength/ductility synergy for additively manufactured Ti-6Al-4V facilitated by machine learning, Mater. Des. 225 (2023) 111559, https://doi.org/10.1016/j.matdes.2022.111559.

[17] TIMET, TIMETAL 6-2-4-6. https://www.timet.com/documents/datasheets/alpha-and-beta-alloys/timetal-6246.pdf. (Accessed January 22, 2024). .

[18] A. Carrozza, A. Aversa, P. Fino, M. Lombardi, A study on the microstructure and mechanical properties of the Ti-6Al-2Sn-4Zr-6Mo alloy produced via laser powder bed fusion, J. Alloys Compd. 870 (2021) 159329, https://doi.org/10.1016/j.jallcom.2021.159329.

[19] I. Weiss, S.L. Semiatin, Thermomechanical processing of beta titanium alloys—an overview, Mater. Sci. Eng., A 243 (1998) 46–65, https://doi.org/10.1016/S0921-5093(97)00783-1.

[20] Y.G. Zhou, W.D. Zeng, H.Q. Yu, An investigation of a new near-beta forging process for titanium alloys and its application in aviation components, Mater. Sci. Eng., A 393 (2005) 204–212, https://doi.org/10.1016/j.msea.2004.10.016.

[21] A. Carrozza, A. Aversa, P. Fino, M. Lombardi, Towards customized heat treatments and mechanical properties in the LPBF-processed Ti-6Al-2Sn-4Zr-6Mo alloy, Mater. Des. 215 (2022) 110512, https://doi.org/10.1016/j.matdes.2022.110512.

[22] H. Peng, S. Wu, W.H. Kan, S.C.V. Lim, Y. Zhu, A. Huang, Rapid hardening response of ultra-hard Ti-6Al-2Sn-4Zr-6Mo alloy produced by laser powder bed fusion, Scripta Mater. 226 (2023) 115209, https://doi.org/10.1016/j.scriptamat.2022.115209.

[23] A. Carrozza, B.A. Bircher, A. Aversa S. Biamino, Investigating complex geometrical features in LPBF-produced parts: a material-based comparison between different titanium alloys, Met. Mater. Int. 29 (2023) 3697–3714, https://doi.org/10.1007/s12540-023-01460-4.

[24] L. Meng, T. Kitashima, T. Tsuchiyama, M. Watanabe, β-Texture evolution during α precipitation in the two-step forging process of a near-β titanium alloy, Metall. Mater. Trans. 51 (2020) 5912–5922, https://doi.org/10.1007/s11661-020-05981-0.

[25] C. Sauer, G. Luetjering, Thermo-mechanical processing of high strength β-titanium alloys and effects on microstructure and properties, J. Mater. Process. Technol. 117 (2001) 311–317, https://doi.org/10.1016/S0924-0136(01)00788-9.

[26] J. Yang, H. Yu, J. Yin, M. Gao, Z. Wang, X. Zeng, Formation and control of martensite in Ti-6Al-4V alloy produced by selective laser melting, Mater. Des. 108 (2016) 308–318, https://doi.org/10.1016/j.matdes.2016.06.117.

[27] X. Gao, G. Abreu Faria, W. Zhang, K.R. Wheeler, Numerical analysis of non-spherical particle effect on molten pool dynamics in laser-powder bed fusion additive manufacturing, Comput. Mater. Sci. 179 (2020) 109648, https://doi.org/10.1016/j.commatsci.2020.109648.

[28] Y. Miyata, M. Okugawa, Y. Koizumi, T. Nakano, Inverse columnar-equiaxed transition (CET) in 304 and 316L stainless steels melt by electron beam for additive manufacturing (AM), Crystals 11 (2021) 856, https://doi.org/10.3390/cryst11080856.

[29] C. Tang, J.L. Tan, C.H. Wong, A numerical investigation on the physical mechanisms of single track defects in selective laser melting, Int. J. Heat Mass Tran. 126 (2018) 957–968, https://doi.org/10.1016/j.ijheatmasstransfer.2018.06.073.

[30] W.F. Gale, T.C. Totemeier, in: W.F. Gale, T.C. Totemier (Eds.), Smithells Metals Reference Book/, eighth ed., Elsevier Butterworth-Heinemann, Oxford, 2004.

[31] M.M. Attallah, S. Zabeen, R.J. Cernik, M. Preuss, Comparative determination of the α/β phase fraction in α+β-titanium alloys using X-ray diffraction and electron microscopy, Mater. Char. 60 (2009) 1248–1256, https://doi.org/10.1016/j.matchar.2009.05.006.

[32] M.H.I. Alluaibi, E.M. Cojocaru, A. Rusea, N. Şerban, G. Coman, V.D. Cojocaru, Microstructure and mechanical properties evolution during solution and ageing treatment for a hot deformed, above β-transus, Ti-6246 alloy, Metals 10 (2020) 1114, https://doi.org/10.3390/met10091114.

[33] A. Piglione, B. Dovgyy, C. Liu, C.M. Gourlay, P.A. Hooper, M.S. Pham, Printability and microstructure of the CoCrFeMnNi high-entropy alloy fabricated by laser powder bed fusion, Mater. Lett. 224 (2018) 22–25, https://doi.org/10.1016/j.matlet.2018.04.052.

[34] B. Zhang, H. Liao, C. Coddet, Microstructure evolution and density behavior of CP Ti parts elaborated by self-developed vacuum selective laser melting system, Appl. Surf. Sci. 279 (2013) 310–316, https://doi.org/10.1016/j.apsusc.2013.04.090.

[35] J. Yang, H. Yu, J. Yin, M. Gao, Z. Wang, X. Zeng, Formation and control of martensite in Ti-6Al-4V alloy produced by selective laser melting, Mater. Des. 108 (2016) 308–318, https://doi.org/10.1016/j.matdes.2016.06.117.

[36] Y. Chong, T. Bhattacharjee, J. Yi, A. Shibata, N. Tsuji, Mechanical properties of fully martensite microstructure in Ti-6Al-4V alloy transformed from refined beta grains obtained by rapid heat treatment (RHT), Scripta Mater. 138 (2017) 66–70, https://doi.org/10.1016/j.scriptamat.2017.05.038.

[37] L. Thijs, M.L. Montero Sistiaga, R. Wauthle, Q. Xie, J.-P. Kruth, J. Van Humbeeck, Strong morphological and crystallographic texture and resulting yield strength anisotropy in selective laser melted tantalum, Acta Mater. 61 (2013) 4657–4668, https://doi.org/10.1016/j.actamat.2013.04.036.

[38] S. Hibino, K. Fujimitsu, M. Azuma, T. Ishimoto, T. Nakano, Effects of recrystallization on tensile anisotropic properties for IN738LC fabricated by laser powder bed fusion, Crystals 12 (2022) 842, https://doi.org/10.3390/cryst12060842.

[39] T. Ishimoto, R. Suganuma, T. Nakano, Tailoring the crystallographic texture of biomedical metastable β-type Ti-alloy produced via laser powder bed fusion using temperature-field simulations, Mater. Lett. 349 (2023) 134835, https://doi.org/10.1016/j.matlet.2023.134835.

[40] T.F. Broderick, A.G. Jackson, H. Jones, F.H. Froes, The effect of cooling conditions on the microstructure of rapidly solidified Ti-6Al-4V, Metall. Trans. A 16 (1985) 1951–1959, https://doi.org/10.1007/BF02662396.

[41] M.C. Lam, S.C.V. Lim, H. Song, Y. Zhu, X. Wu, A. Huang, Scanning strategy induced cracking and anisotropic weakening in grain texture of additively manufactured superalloys, Addit. Manuf. 52 (2022) 102660, https://doi.org/10.1016/j.addma.2022.102660.

[42] J.D. Hunt, Steady state columnar and equiaxed growth of dendrites and eutectic, Mater. Sci. Eng., A 65 (1984) 75–83, https://doi.org/10.1016/0025-5416(84)90201-5.

[43] J. Yang, H. Yu, J. Yin, M. Gao, Z. Wang, X. Zeng, Formation and control of martensite in Ti-6Al-4V alloy produced by selective laser melting, Mater. Des. 108 (2016) 308–318, https://doi.org/10.1016/j.matdes.2016.06.117.

[44] S.K. Shaha, H. Jahed, J. Kacher, Additively manufactured Ti55511 alloy: microstructure and residual stress effect on mechanical properties, J. Manuf. Process. 94 (2023) 348–358, https://doi.org/10.1016/j.jmapro.2023.03.039.

[45] J. Liao, C. Ye, B.J. Kim, S. Suslov, E.A. Stach, G.J. Cheng, Nucleation of highly dense nanoscale precipitates based on warm laser shock peening, J. Appl. Phys. 108 (2010) 063518, https://doi.org/10.1063/1.3481858.

[46] M.T. Jovanović, S. Tadić, S. Zec, Z. Mišković, I. Bobić, The effect of annealing temperatures and cooling rates on microstructure and mechanical properties of investment cast Ti–6Al–4V alloy, Mater. Des. 27 (2006) 192–199, https://doi.org/10.1016/j.matdes.2004.10.017.

[47] S.C. Wang, M. Aindow, M.J. Starink, Effect of Self-accommodation on α/α boundary populations in pure titanium, Acta Mater. 51 (2003) 2485–2503, https://doi.org/10.1016/S1359-6454(03)00035-1.

[48] T. Song, T. Dong, S.L. Lu, K. Kondoh, R. Das, M. Brandt, M. Qian, Simulation-informed laser metal powder deposition of Ti-6Al-4V with ultrafine α-β lamellar structures for desired tensile properties, Addit. Manuf. 46 (2021) 102139, https://doi.org/10.1016/j.addma.2021.102139.

[49] A.L. Otte, P.T. Mai, A. Stark, M. Hoelzel, M. Hofmann, J. Gibmeier, Kinetics of martensite decomposition and microstructure stability of Ti-6246 during rapid heating to service temperatures, Metals 13 (2023) 484, https://doi.org/10.3390/met13030484.

[50] M.A. Buhairi, F.M. Foudzi, F.I. Jamhari, A.B. Sulong, N.A.M. Radzuan, N. Muhamad, I.F. Mohamed, A.H. Azman, W.S.W. Harun, M.S.H. Al-Furjan, Review on volumetric energy density: influence on morphology and mechanical properties of Ti6Al4V manufactured via laser powder bed fusion, Prog. Addit. Manuf. 8 (2023) 265–283, https://doi.org/10.1007/s40964-022-00328-0.

[51] S. Hibino, T. Todo, T. Ishimoto, O. Gokcekaya, Y. Koizumi, K. Igarashi, T. Nakano, Control of crystallographic texture and mechanical properties of hastelloy-X via laser powder bed fusion, Crystals 11 (2021) 1064, https://doi.org/10.3390/cryst11091064.

[52] T. DebRoy, H.L. Wei, J.S. Zuback, T. Mukherjee, J.W. Elmer, J.O. Milewski, A. M. Beese, A. Wilson-Heid, A. De, W. Zhang, Additive manufacturing of metallic components - process, structure and properties, Prog. Mater. Sci. 92 (2018) 112–224, https://doi.org/10.1016/j.pmatsci.2017.10.001.

[53] X. Zhu, Z. Zhu, T. Liu, W. Liao, Y. Du, H. Wei, Crack-free and high-strength AA2024 alloy obtained by additive manufacturing with controlled columnar-equiaxed-transition, J. Mater. Sci. Technol. 156 (2023) 183–196, https://doi.org/10.1016/j.jmst.2023.01.012.

[54] X. Niu, H. Shen, J. Fu, J. Feng, Effective control of microstructure evolution in AZ91D magnesium alloy by SiC nanoparticles in laser powder-bed fusion, Mater. Des. 206 (2021) 109787, https://doi.org/10.1016/j.matdes.2021.109787.

[55] A. Takase, T. Ishimoto, R. Suganuma, T. Nakano, Surface residual stress and phase stability in unstable β-type Ti-15Mo-5Zr-3Al alloy manufactured by laser and electron beam powder bed fusion technologies, Addit. Manuf. 47 (2021) 102257, https://doi.org/10.1016/j.addma.2021.102257.

[56] S. Huanga, P. Kumar, W.Y. Yeong, R. Narayan, U. Ramamurty, Fracture behavior of laser powder bed fusion fabricated Ti41Nb via in-situ alloying, Acta Mater. 225 (2022) 117593, https://doi.org/10.1016/j.actamat.2021.117593.

[57] Y. Zhu, X. Wu, Perspective on hetero-deformation induced (HDI) hardening and back stress, Mater. Res. Lett. 7 (2019) 393–398, https://doi.org/10.1080/21663831.2019.1616331.